Generation of biaxially accelerating static Airy light-sheets with 3D-printed freeform micro-optics

Yanis Taege [iD],[a] **Tim Samuel Winter,**[a] **Sophia Laura Schulz,**[b] **Bernhard Messerschmidt,**[b] and **Çağlar Ataman**[c,*]
[a]University of Freiburg, Department of Microsystems Engineering, Laboratory for Micro-Optics, Freiburg, Germany
[b]GRINTECH GmbH, Jena, Germany
[c]University of Freiburg, Department of Microsystems Engineering, Microsystems for Biomedical Imaging Laboratory, Freiburg, Germany

Abstract. One-dimensional Airy beams allow the generation of thin light-sheets without scanning, simplifying the complex optical arrangements of light-sheet microscopes (LSMs) with an extended field of view (FOV). However, their uniaxial acceleration limits the maximum numerical aperture of the detection objective in order to keep both the active and inactive axes within the depth of field. This problem is particularly pronounced in miniaturized LSM implementations, such as those for endomicroscopy or multi-photon neural imaging in freely moving animals using head-mounted miniscopes. We propose a new method to generate a static Airy light-sheet with biaxial acceleration, based on a novel phase profile. This light-sheet has the geometry of a spherical shell whose radius of curvature can be designed to match the field curvature of the micro-objective. We present an analytical model for the analysis of the light-sheet parameters and verify it by numerical simulations in the paraxial regime. We also discuss a micro-optical experimental implementation combining gradient-index optics with a 3D-nanoprinted, fully refractive phase plate. The results confirm that we are able to match detection curvatures with radii in the range of 1.5 to 2 mm.

Keywords: light-sheet microscopy; Airy beam; accelerating beams; field curvature; two-photon polymerization.

1 Introduction

Light-sheet fluorescence microscopy (LSM) has become an essential imaging modality in the life sciences, providing rapid volumetric imaging with minimal photodamage.[1] Although this makes it an ideal candidate for *in vivo* imaging, such as endo-microscopy[2,3] and neural imaging in freely moving animals,[4,5] translation to miniaturized optical systems has been limited to date.[6,7] A critical technology for incorporating LSM into these applications is high-performance micro-objectives that can match their macroscopic counterparts in numerical aperture (NA) and field of view (FOV).[8] Their performance comes at the cost of field curvature,[9,10] which presents an additional challenge for LSM. With the generally planar geometry of a Gaussian beam, only a limited portion of the illuminated area is brought into perfect focus in the image plane, limiting the effective FOV,

imposing limits on the detection NA, or leading to loss in image contrast. Although the incorporation of scanning micromirrors could address this challenge to some extent,[11] this further increases the system complexity and limits the achievable degree of miniaturization. Using Airy beams[12] has been proposed to match field curvature due to its uniaxial acceleration when implemented as a static light-sheet.[13] An Airy light-sheet can be generated by imposing a one-dimensional (1D) cubic phase profile on a Gaussian beam, which is then focused by a cylindrical lens. Similar to other configurations using propagation-invariant beams,[14,15] it has been used to excite a larger FOV compared to a Gaussian sheet, while maintaining the same sectioning ability.[16,17] However, incorporating the static Airy light-sheet only partially solves the curvature problem, as the planar Gaussian profile along its inactive axis still introduces an FOV reduction, limiting the performance required for micro-optical applications.

We have recently shown that this challenge can be addressed by an additional phase modulation on top of the cubic profile needed for the static Airy sheet.[18] This phase profile depends linearly on the active coordinate and quadratically on the inactive coordinate and modifies the Gaussian profile of the light-sheet to achieve the same radius of curvature as the Airy beam. The result is a static, biaxially accelerating light-sheet that is unrestricted in its ability to section, thus increasing the effective FOV of the micro-objective. In this paper, we provide a detailed analytical derivation of the phase-plate parameterization using typical micro-objective specifications, allowing the light-sheet geometry to be tailored for maximized in-focus excitation. To verify the validity of our analysis, we perform simulations in the paraxial regime using ray-tracing and beam-propagation methods (BPMs). By designing, implementing, and characterizing a micro-optical excitation system that incorporates a 3D-printed millimeter-scale phase plate, we experimentally demonstrate our ability to generate such a light-sheet in a fully miniaturized fashion.

2 Theory

Figure 1(a) shows the optical architecture of a miniaturized light-sheet microscope with a high NA micro-objective. The illumination arm consists of a collimator (not shown) and a cylindrical lens to form a Gaussian light-sheet within the FOV of the micro-objective that is imaging the excited fluorescence onto a flat image sensor. The field curvature of the detection objective z_d can be characterized by a radius $r_d \gg$ FOV so that the detection field follows:

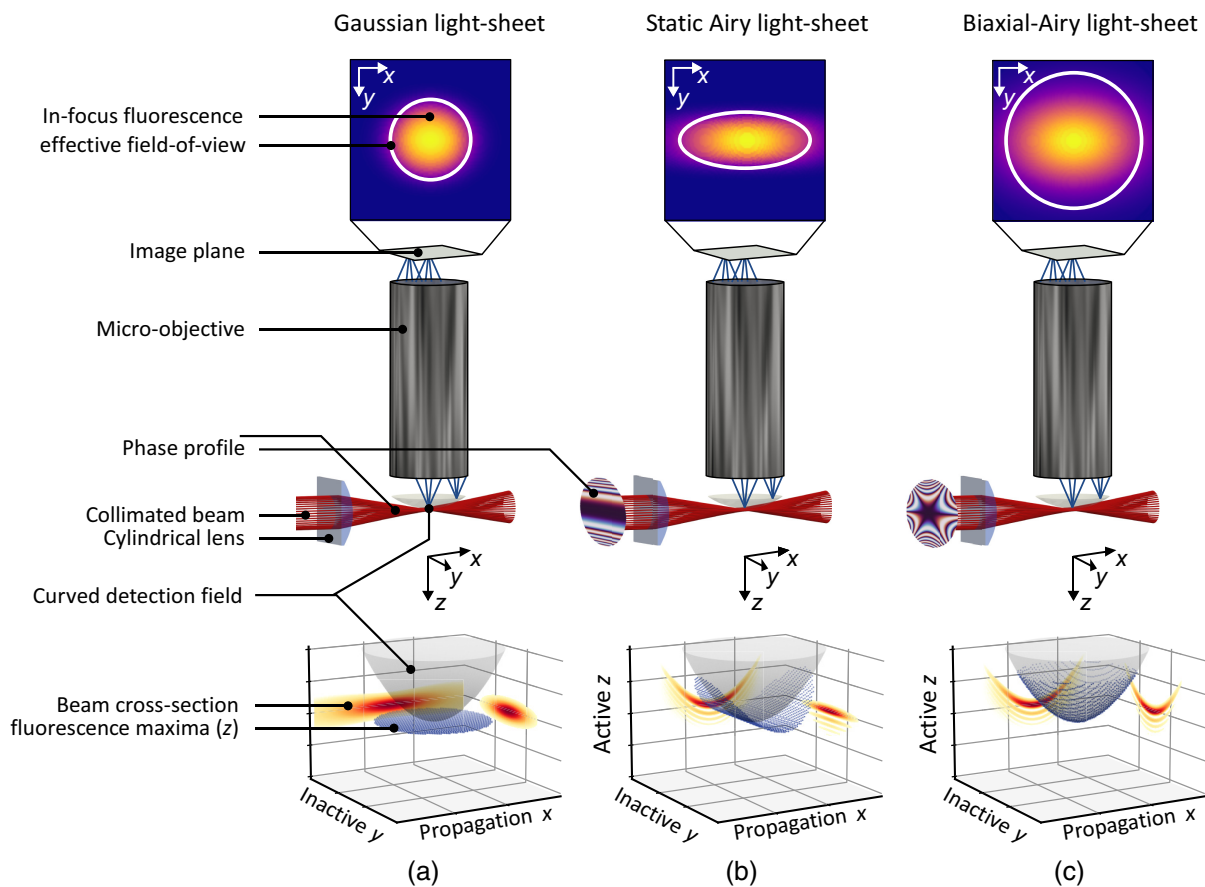$$z_\mathrm{d}(x, y) \approx \frac{x^2 + y^2}{2r_d}. \tag{1}$$

Fig. 1 Comparison of three different static light-sheet illumination beams for a typical micro-objective for a given light-sheet length and detection NA. The detected in-focus fluorescence, which is imaged by the micro-objective with a curved detection field (gray cone, center) onto the image plane, is plotted on the top. In the bottom row, the intensity profiles of the illumination beams are plotted in cross sections along the center in the propagation coordinate (XZ-plane, to the back) and the focal plane (XY-plane, to the right). A blue mesh traces the maximum intensity of the beams along the detection axes, visualizing the mismatch between beam- and detection field-geometry. (a) Gaussian light-sheet. Due to its planar geometry, the in-focus fluorescence is significantly smaller than that of the available FOV. (b) Static Airy light-sheet. Due to the matched curvature along the propagation axis, the effective FOV is increased. In addition, the Airy beam is thinner than the Gaussian beam with the same FOV. (c) Proposed biaxial Airy beam. By adjusting the curvature also along the inactive direction, the fluorescence collection over the entire illumination area will be in focus.
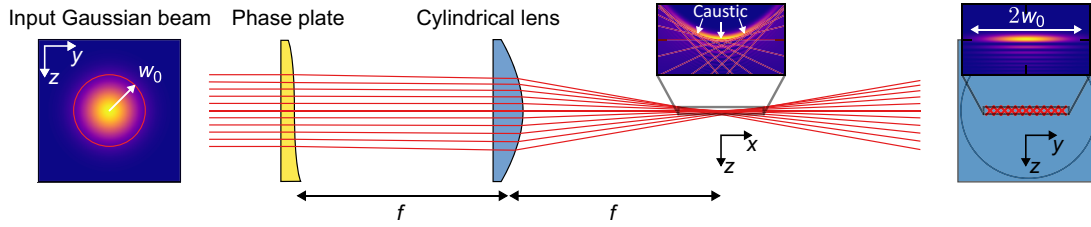
Fig. 2 Configuration to generate a 1D-Airy light-sheet to illustrate the mathematical derivation. An input Gaussian beam with a beam waist of w_0 is modulated by a 1D cubic phase plate. The phase plate is placed in the BFP of a cylindrical lens that focuses the beam in the z coordinate. The resulting beam profiles, illustrated by the insets in the XZ and YZ planes, show an Airy profile in the z- and a Gaussian profile in the y-coordinate.

As common in LSM, we use the coordinate system of the detection objective for the light-sheet, in which

- z is the micro-objective's optical axis, corresponding to the cylindrical lens' active axis,
- x is the optical axis of the cylindrical lens corresponding to the beam propagating direction, and
- y is the inactive coordinate of the cylindrical lens.

Figure 1(b) extends the concept to the generation of a static Airy light-sheet, resulting from a 1D cubic phase modulation of the collimated beam incident on the cylindrical lens, which allows field curvature matching in x. This already increases the effective FOV in this coordinate compared with the Gaussian light-sheet and improves the sectioning capability due to a thinner light-sheet. A secondary phase modulation of the proposed phase profile aims at bending the Airy light-sheet along its inactive axis, thus generating a static and yet biaxially accelerating sheet [Fig. 1(c)]. In the next two sections, we discuss the design of the active and inactive phase profiles to achieve biaxial field curvature matching.

2.1 Acceleration along the Propagation Direction

An Airy light-sheet can be generated by modulating the collimated Gaussian beam with a beam waist w_0 by a 1D cubic phase ϕ_{Ai} at the back focal plane (BFP) of the cylindrical lens[13] along its active direction z, such that the electric field follows,

$$E_{\mathrm{Ai}}^{\mathrm{BFP}}(y,z) = \exp\left(-\frac{z^2 + y^2}{w_0^2}\right) \cdot \exp\left[i2\pi\alpha\left(\frac{z}{w_0}\right)^3\right], \quad (2)$$

where α is the amplitude of cubic modulation. A schematic depiction of this configuration is shown in Fig. 2, where the approximate intensity profile around the focal plane can be obtained in the paraxial domain as[19,20]

$$I_{\mathrm{Ai}}(x,y,z) \approx \left|\mathrm{Ai}\left(\frac{z}{z_0} - \frac{x^2}{2r_{\mathrm{Ai}}z_0} + i\frac{ax}{kz_0^2}\right)\right|^2$$
$$\cdot \exp\left[2a\left(\frac{z}{z_0} - \frac{x^2}{r_{\mathrm{Ai}}z_0}\right) - \frac{2y^2}{w_0^2}\right], \quad (3)$$

where $\mathrm{Ai}(\cdot)$ denotes the Airy function, x is the axial coordinate, $z_0 = f(6\pi\alpha)^{\frac{1}{3}}/(w_0 k)$ is a characteristic length, $a = (6\pi\alpha)^{-2/3}$ is an apodization factor, and $k = 2\pi n/\lambda$ is the wave vector in a medium of refractive index n.[21] It has been demonstrated by numerous research groups[19,22–25] that this function is highly

asymmetrical with prominent sidelobes, and its main lobe follows a parabola with a radius of curvature r_{Ai} of

$$r_{\mathrm{Ai}} = \frac{6\lambda n^2 f^3}{w_0^3}\alpha. \quad (4)$$

Therefore, one must solve Eq. (4) for α with $r_{\mathrm{Ai}} = r_d$ to obtain an Airy light-sheet with an acceleration matching the field curvature of the detection objective. Using Eq. (2), we obtain

$$\phi_{\mathrm{Ai}}(z) = \frac{2\pi r_d}{6\lambda n^2 f^3} \cdot z^3. \quad (5)$$

To finalize the geometry of the light-sheet, the beam needs to be matched to the FOV of the micro-objective, which we define as the area around the focal point within which the intensity remains larger than the half of the maximum value.[21] Since Eq. (5) does not depend on w_0, we can control the geometry of the light-sheet in the propagation coordinate and in the inactive coordinate independently of each other via the focal length and the beam waist. Explicitly, the FOV along the active direction is obtained from

$$\mathrm{FOV}_x = \frac{w_0 r_d \sqrt{2\ln 2}}{nf}, \quad (6)$$

and along the inactive direction from

$$\mathrm{FOV}_y = \sqrt{2\ln 2}\, w_0. \quad (7)$$

To obtain a symmetric FOV, the condition $r_d = nf$ must be satisfied, which means that the focal length in the imaging medium must be equal to the radius of curvature.

2.2 Acceleration along the Inactive Direction

To induce a parabolic axial shift of the focal point along the inactive coordinate y as well, we modify Eq. (3) by convolving it with a delta distribution $\delta(\cdot)$ with the required shift in the detection coordinate. This operation can be expressed as

$$I_{\mathrm{biaxial}}(x,y,z) = I_{\mathrm{Ai}}(x,y,z) \circledast \delta\left(z - \frac{y^2}{2r_d}\right), \quad (8)$$

$$\approx \left|\mathrm{Ai}\left(\frac{z}{z_0} - \frac{x^2 + y^2}{2r_d z_0} + i\frac{ax}{kz_0^2}\right)\right|^2$$
$$\cdot \exp\left[2a\left(\frac{z}{z_0} - \frac{2x^2 + y^2}{2r_d z_0}\right) - \frac{2y^2}{w_0^2}\right], \quad (9)$$

where ⊛ denotes the convolution operation. Details of this derivation can be found in Appendix A. By taking the Fourier transform of the electric field at the focal point $x = 0$ along z, we can again obtain the required electric field at the BFP, which can be approximated as

$$E_{\text{biaxial}}^{\text{BFP}}(y, z) \approx \exp\left(-\frac{z^2 + y^2}{w_0^2}\right) \cdot \exp\left[i2\pi\alpha\left(\frac{z}{w_0}\right)^3\right]$$
$$\cdot \exp\left(-i\frac{\pi}{r_d\lambda f} \cdot y^2 z\right). \tag{10}$$

The arguments of the first two exponential functions in Eq. (10) represent the conventional profile to generate an Airy beam as per Eq. (2), while the last term is an additional, phase-only term that we define as

$$\phi_{\text{inactive}}(y, z) = -\frac{\pi}{r_d\lambda f} \cdot y^2 z. \tag{11}$$

In ray optical terms, this phase profile adds an additional launch angle from the phase plate to the cylindrical lens in its active coordinate, the magnitude of which varies as the square of the inactive coordinate. Because of the introduction of this additional angle in the BFP, each 1D Airy ray will be shifted in z at the focal plane of the cylindrical lens.

2.3 Combined Phase Profile

A combined phase plate with a sag height of h_{PP}, which generates both the 1D Airy beam along the propagation coordinate, as well as the focus-shifted Gaussian beam along the inactive coordinate of the beam, can be obtained as

$$h_{\text{PP}}(y, z) = \frac{\lambda \cdot (\phi_{\text{Ai}} + \phi_{\text{inactive}})}{2\pi(n_m - 1)}, \tag{12}$$

$$= \frac{r_d}{6n^2 f^3(n_m - 1)} z^3 - \frac{1}{2r_d f(n_m - 1)} y^2 z, \tag{13}$$

where n_m is the refractive index of the phase plate. The individual profiles are plotted alongside the combined one in Fig. 3. An important point about Eq. (13) is that the Airy-related modulation scales linearly with r_d, while the modulation related to the inactive profile is inversely proportional to it. This imposes a limit on the range of r_d that can be realized. For lower values of r_d, the α parameter is smaller, and the assumptions made in the derivation of the apodized Airy beam become invalid.[19,25] On the other hand, the modulation generated by the inactive profile dominates the phase plate. This leads to larger launch angles, which may violate the paraxial approximation of the optical element. At the upper end of the limit, it is useful to evaluate whether field curvature remains a problem as the beam becomes flatter and thicker, bypassing the initial problem.

3 Methods

3.1 Simulations

To assess that curvature-matching in the paraxial regime, we performed ray-tracing simulations using commercial software (OpticStudio 22.1, Zemax LLC). The simulation model
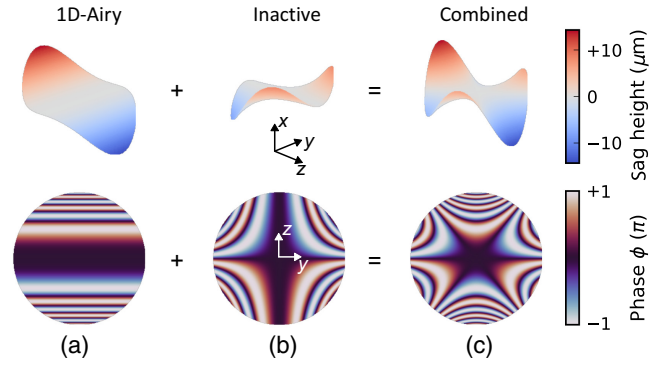

Fig. 3 Schematic illustration of the combined phase plate profiles for a diameter of 1 mm. (a) Cubic profile ϕ_{Ai} along the active direction of the cylindrical lens to generate the 1D-Airy beam. (b) Inactive profile ϕ_{inactive} that adds a linear phase along the active direction, whose slope depends quadratically on the inactive direction of the cylindrical lens. This profile leads to a focal shift in the active coordinate such that it follows the same acceleration as the one induced by the cubic profile. (c) Linear combination of the individual profiles that generates the biaxially accelerating light-sheet as given in Eq. (13).

implemented the configuration shown in Fig. 2, with the phase profile described in Sec. 2.3. We calculated the curvature of the beam in the active direction by evaluating the caustic[26] of 51 rays displaced in the active z-coordinate (XZ-section in Fig. 2). For the inactive direction, we obtained the displacement of the rays in the image plane by tracing 51 rays that were initially displaced along the y-direction. To further investigate the validity of Eq. (9), we propagated the field defined in Eq. (10) using a 2D fast Fourier transform (FFT) based BPM in the Fresnel regime.[21] Propagation was performed to match the ray-tracing simulations, which included the same beam waist, phase plate profile, and focal length of the cylindrical lens. 3D stacks were calculated within a range of ±300 μm around the focal point with a step size of $\Delta z = 5$ μm, and a grid size of $(n_x \times n_y) = (2^{12} \times 2^{12})$ pixels with a width of $\Delta x = \Delta y = 0.2$ μm. We set the input parameters with an excitation wavelength $\lambda = 850$ nm, an input beam waist $w_0 = 240$ μm, an effective focal length of the cylindrical lens $f_z = 1.4$ mm, and a refractive index of the phase plate $n_m = 1.509$[27] to match the experimental setup described below. Two radii of curvature were chosen in a typical range for micro-objectives of 1.5 and 2 mm.[8,9,28]

3.2 Fabrication and Characterization

Phase plates with a diameter of 0.78 mm were fabricated using a commercial two-photon polymerization based 3D printer (PPGT+, Nanoscribe GmbH & Co KG) with a commercial resin (IPS, NanoScribe GmbH & Co KG). The height profiles were pre-processed and subsequently fabricated on ITO-coated glass substrates using an in-house developed slicing and printing strategy, previously described.[29] After development, the height profiles of the phase plates were measured by white-light interferometry (WLI; NewView 9000, Zygo Corporation). A 0.3-NA objective (I100384, Zygo Cooperation) was used to obtain the surface profile of the entire plate and then fitted with standard Zernike polynomials to quantify the shape deviation. Since the tilt of the printing field in this system can only be controlled to
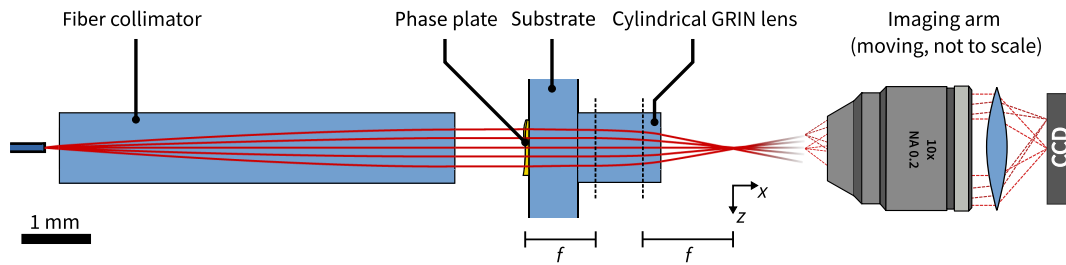
Fig. 4 Experimental setup used to measure the biaxially accelerating beam profiles following the configuration in Fig. 2. For a micro-optical implementation, input beam shaping is performed by a fiber-based collimation unit. The glass substrate on which the phase plate has been fabricated features a cylindrical GRIN lens at its back that focuses the modulated beam from its BFP to the focal plane. Around this plane, the light-sheet is imaged by moving an imaging arm, consisting of a 0.2-NA detection objective, a relay lens, and a CCD, in the propagation direction of the beam.

within a few micrometers from print to print, the tilt Zernike coefficients were not included in the deviation analysis. The surface roughness was estimated by measuring a $25 \ \mu m \times 25 \ \mu m$ area of the phase plate with a 0.8-NA objective (I190053, Zygo Cooperation). A high-pass Gaussian spline filter with a cutoff frequency of $25 \ \mu m$ was applied and the resulting root mean square (RMS) error was calculated.[30]

3.3 Experimental Setup and Analysis of the Beam Profiles

A cylindrical gradient-index (GRIN) lens with an effective focal length of 1.4 mm (Grintech GmbH) was bonded to the back of the substrate after fabrication so the phase plate was located at its BFP. The entire assembly was illuminated with a fiber-based collimator (GRINTECH GmbH) using an SLED with a wavelength of 850 nm as the light source (Fig. 4). The beam waist of the illumination beam after the collimator was $w_0 = 240 \ \mu m$. In order to obtain the 3D beam profile in the vicinity of the focal plane of the cylindrical lens, the beam was imaged onto a CCD (UI-1240SE-NIR, IDS GmbH) using a 0.28-NA objective (Plan Apo 10x, Mitutoyo AC) and a relay lens, while the entire system was translated along the propagation direction of the light-sheet.

To compare the analytical analysis, simulations, and experiments, 2D cross sections of the beam intensity along its propagation direction at ($y = 0$) and along the inactive direction at the focal plane ($x = 0$) were measured. The thickness Δz and the $FOV_{x,y}$ were determined by finding the full width at half-maximum of the beam intensity in the respective direction. The radius of curvature in x and y was determined by finding the location of the maximum intensity in the respective coordinate and fitting Eq. (1) to these data points using a least-squares algorithm.[31]

4 Results

Figure 5 shows the characterization of the surface profile obtained with the WLI. The surface errors become more pronounced toward the edge, where lift-off from the substrate is expected, but were found to be $<1 \ \mu m$ over a diameter of $780 \ \mu m$. With an RMS surface roughness below 10 nm, the phase plate can be considered an optical quality surface.

Table 1 compares the radii of curvature determined by Eq. (9), ray-tracing and BPM simulations with the experimental measurements. The ray-tracing simulations yielded radii of
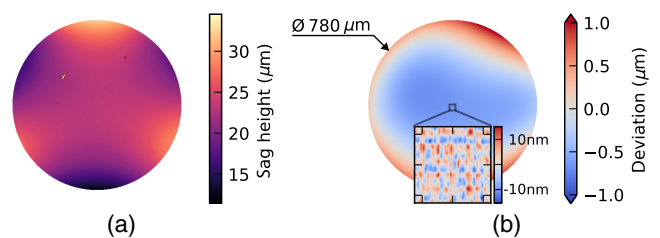

Fig. 5 Characterization of the phase plate profile with $r_d = 2$ mm using white-light-interferometry. (a) The measured surface profile, and (b) the tilt-corrected deviation from the ideal surface i. The inset on the right provides the high-pass filtered, high-NA scan for roughness estimation.

Table 1 Comparison of the radii of curvature determined by Eq. (9), ray-tracing and BPM simulations with the experimental measurements. The corresponding beam profiles of the latter three are also shown in Fig. 6. Since the differences between the analytical and ray-tracing results are within the limits of numerical accuracy, they are not shown explicitly.

Design Radius		Active Coordinate (mm)	Inactive Coordinate (mm)
$r_d = 1.5$ mm	Analytical	1.5	1.5
	Simulation (ray-tracing)	1.5	1.5
	Simulation (BPM)	(1.5 ± 0.1)	(1.4 ± 0.1)
	Experiment	(1.3 ± 0.1)	(1.4 ± 0.1)
$r_d = 2.0$ mm	Analytical	2.0	2.0
	Simulation (ray-tracing)	2.0	2.0
	Simulation (BPM)	(2.1 ± 0.1)	(2.0 ± 0.1)
	Experiment	(2.0 ± 0.1)	(1.8 ± 0.1)

curvature that matched the design radii within numerical accuracy. Furthermore, the simulated beam profiles shown in Fig. 6 agree with those generated by evaluating Eq. (9). Deviations can be narrowed down to an asymmetric intensity distribution
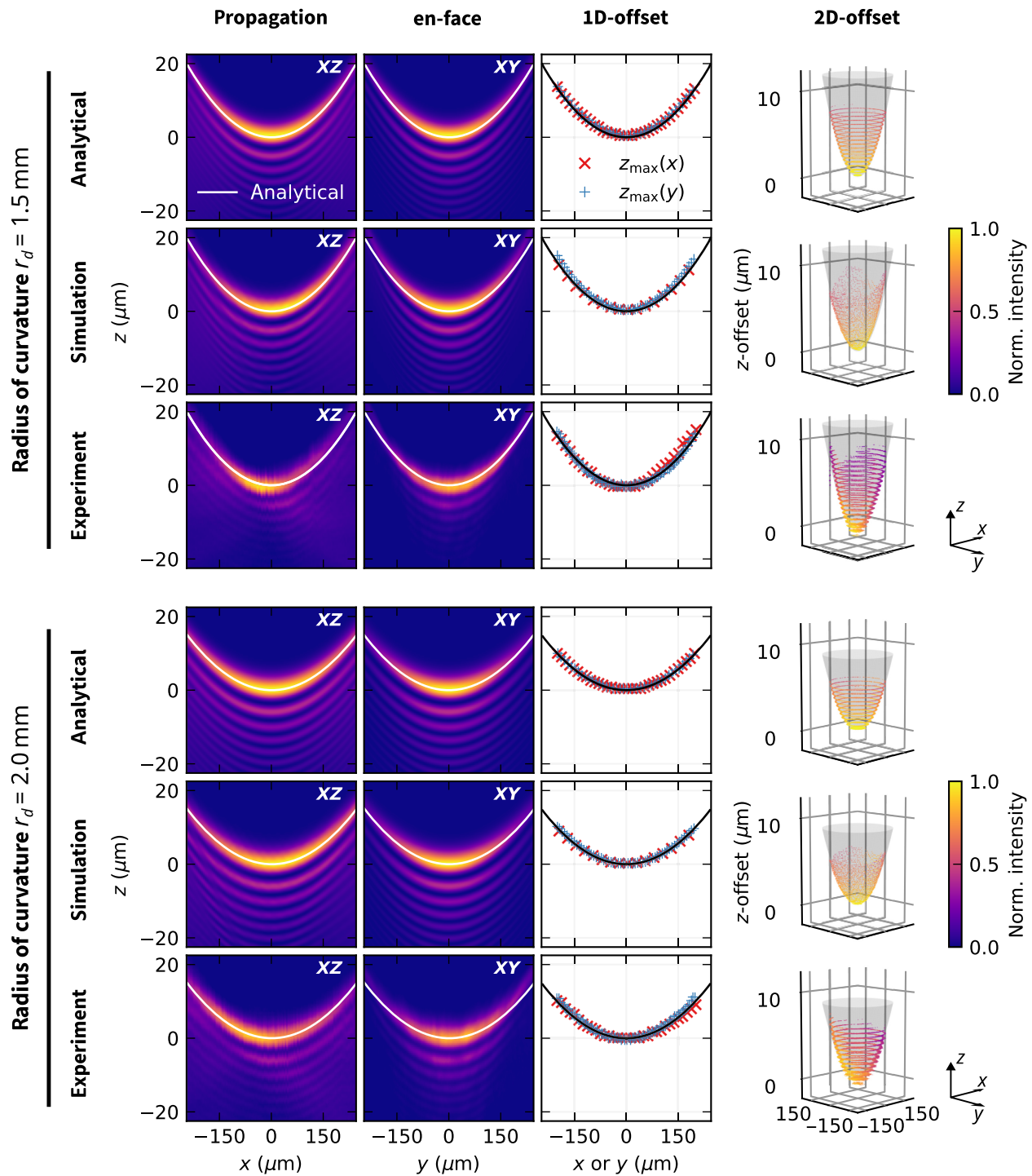
Fig. 6 Biaxially accelerating beam profiles obtained by the analytical evaluation [Eq. (9)], the BPM simulations, and the beam profiling experiments. The central cross sections of the beam in propagation direction (XZ-plane) and along the inactive coordinate (XY-plane) are plotted and show the typical Airy profiles of the beam, though with an acceleration also along the latter coordinate. The z-offsets of the intensity maxima are plotted in x and y of directions both 1D cross sections. To also show that the main lobe's intensity resembles a spherical cap, the z-offsets are plotted along both dimensions simultaneously and color-coded with the respective intensity. The evolution of the design radii is shown alongside each plot.

around the focus below 10 μm, and predicted offsets in z are consistent with both design and numerical predictions. The radii of curvature obtained from measured data matched the design values in most cases. For $r_d = 1.5$ mm, the radii in the propagation coordinate and in the inactive coordinate were found to be (0.2 ± 0.1) mm and (0.1 ± 0.1) mm smaller than the design value, respectively. For $r_d = 2.0$ mm, the radius of the active coordinate is equal to the designed radius, while the inactive coordinate is (0.2 ± 0.1) mm smaller than the designed radius. The beam profiles themselves show the typical Airy profiles, although a reduced sidelobe intensity is observed with an underestimation of the FOV in the propagation direction from 20% to 36% and 5% to 10% in the inactive coordinate.

5 Discussion and Conclusions

The excellent agreement between the results of our analytical treatment and the ray-traced simulations is a good indication of the validity of the design approach within the paraxial regime. Limitations of this approximation may arise in different scenarios. As discussed in Sec. 2.3, lower values of r_d will lead to a reduced modulation of the Airy profile. Therefore, we expect the radius to be underestimated in the propagation coordinate, as observed in the experimental data. In the inactive direction, we also expect to see an underestimated radius, but for a different reason. The higher additional deflection leads to a gradual violation of the paraxial approximation, resulting in aberrations and thus lower radii. On the other hand, we observed the Airy radius to be the same as the design radius for larger values of r_d, whereas the radius along the inactive direction is slightly smaller. We attribute this to a manufacturing effect as for smaller values of r_d, the sag height decreases and therefore requires more accurate manufacturing capabilities. Both effects can lead to the deviations reflected in the experimental results. Nevertheless, we have been able to adjust both radii to a degree that does not affect the improvement in effective FOV, which was the underlying design goal.

In summary, we have derived a phase profile to generate an Airy light-sheet that follows the curved image plane of a typical micro-objective, while incorporating the advantages of using an Airy beam to provide a larger FOV and better sectioning. Raytracing and BPM simulations in the paraxial regime validated the analytical analysis, with deviations between the two within numerical accuracy. A micro-optical implementation with milimeter-scale 3D-printed refractive phase plate was developed and combined with GRIN lens and experimentally demonstrated to achieve curvature matching in the design range.

6 Appendix A: Derivation of the Phase Profile

To obtain the required phase profile, we need an expression of the biaxial electric field at the focal plane $x = 0$, which we can approximate from the apodized Airy beam convoluted by the delta distribution δ as in Eq. (9) such that

$$E_{\text{biaxial}}(x = 0, y, z) = \text{Ai}\left(\frac{z}{z_0}\right) \cdot \exp\left(\frac{az}{z_0} - \frac{y^2}{w_0^2}\right) \circledast \delta\left(z - \frac{y^2}{2r_d}\right).$$
(14)

The electric field at the BFP can be obtained by taking the Fourier transform along the active direction of the lens $\mathcal{F}_z\{\cdot\}$, i.e.,

$$E_{\text{biaxial}}^{\text{BFP}}(y, z) = \mathcal{F}_z\left\{\text{Ai}\left(\frac{z}{z_0}\right) \cdot \exp\left(\frac{az}{z_0} - \frac{y^2}{w_0^2}\right) \circledast \delta\left(z - \frac{y^2}{2r_d}\right)\right\}.$$
(15)

Since the Gaussian component is only dependent on y, it is neither affected by $\mathcal{F}_z$, nor by the delta distribution and can thus be separated,

$$E_{\text{biaxial}}^{\text{BFP}}(y, z) = \mathcal{F}_z\left\{\text{Ai}\left(\frac{z}{z_0}\right) \cdot \exp\left(\frac{az}{z_0}\right) \circledast \delta\left(z - \frac{y^2}{2r_d}\right)\right\}$$
$$\cdot \exp\left(-\frac{y^2}{w_0^2}\right).$$
(16)

Using the convolution theorem, we can also simplify the convolution operation to a product, such that $\mathcal{F}_z$ operates individually on the apodized Airy function, whose identity is known from Eq. (2). The Fourier transform of a linear delta distribution is an exponential function,

$$\mathcal{F}_z\left\{\delta\left(z - \frac{y^2}{2r_d}\right)\right\} \propto \exp\left(-i\frac{k_z y^2}{2r_d}\right),$$
(17)

where $k_z \approx 2\pi z/(\lambda f)$ is the wave vector in the active coordinate. Inserting those identities into Eq. (16) leaves

$$E_{\text{biaxial}}^{\text{BFP}}(y, z) = \mathcal{F}_z\left\{\text{Ai}\left(\frac{z}{z_0}\right) \cdot \exp\left(\frac{az}{z_0}\right)\right\} \cdot \mathcal{F}_z\left\{\delta\left(z - \frac{y^2}{2r_d}\right)\right\}$$
$$\cdot \exp\left(-\frac{y^2}{w_0^2}\right),$$
(18)

$$\approx \exp\left(-\frac{z^2}{w_0^2}\right) \cdot \exp\left[i2\pi\alpha\left(\frac{z}{w_0}\right)^3\right] \cdot \exp\left(-i\frac{\pi}{r_d\lambda f} \cdot y^2 z\right)$$
$$\cdot \exp\left(\frac{-y^2}{w_0^2}\right),$$
(19)

$$= \exp\left(-\frac{z^2 + y^2}{w_0^2}\right) \cdot \exp\left[i2\pi\alpha\left(\frac{z}{w_0}\right)^3\right] \cdot \exp\left(-i\frac{\pi}{r_d\lambda f} \cdot y^2 z\right),$$
(20)

which is a Gaussian beam (the first exponential function) on which the cubic Airy phase (the second exponential argument) as well as the biaxial tilt (the third exponential argument) is imposed.

We would like to underline the fact that several assumptions were made in the derivation of Eq. (20) which can be summarized by the following points:

- The Rayleigh range of the input Gaussian beam is much larger than the propagation distance from the backfocal to the focal plane of the lens, i.e., $x_r \gg 2f$. This ensures that the light-sheet does not expand in y.

- All approximations made are strictly in the paraxial regime, such that the Abbe sine condition is fulfilled, i.e., $k_z/k \approx z/f$.

• There are several approximations made for the expression of the Airy beam, of which one is that the apodization a must be sufficiently strong, i.e., $a \ll 1$. For our application, this condidition is reasonably fulfilled if $\alpha > 2$.

• All calculations are strictly proportionalities (e.g., constants like the impedance or scaling factors like $\sqrt{2\pi}$ are not mentioned explicitly).

Any violation of those assumptions may result in aberrations of the Airy beam, which leads to a variation in length and thickness of the light-sheet, and in mismatch of the field curvature, as discussed in Section 5.

7 Appendix B: Other Inactive Geometries

In general, the argument of the δ function in Eq. (20) can be modified to resemble an arbitrary focal shift in z depending on a function $g(y)$, i.e.,

$$s(z, y) = \delta[z - g(y)]. \tag{21}$$

An example for a benchtop application is the combination of a spatial light modulator (SLM) with a cylindrical lens to generate a 1D-Airy light-sheet. If the imaging arm is rolled with respect to the detection arm, the light-sheet will intersect the focal plane at an angle. By setting $g(y)$ to match this tilt, one can compensate this misalignment without moving any mechanical components by employing a phase of

$$\phi_{\text{inactive}} = k_z \cdot g(y), \tag{22}$$

onto the SLM.

8 Appendix C: Further Detailed Results

Table 2 accompanies the results presented in Table 1 by additionally stating the length and thickness of the light-sheet.

Table 2 Detailed results accompying those in Table 1. In addition to the radii of curvatures, the FOV$_{x,y}$ in each direction is given, as well as the thickness of the light-sheet Δz.

Design Radius		Active x		Active y		
		r_x (mm)	FOV$_x$ (μm)	r_y (mm)	FOV$_y$ (μm)	Δz (μm)
$r_d =$ 1.5 mm	Analytical	1.5	354	1.5	299	4.0
	Ray-tracing	1.5	—	1.5	—	—
	BPM	(1.5 ± 0.1)	362	(1.4 ± 0.1)	301	4.0
	Experiment	(1.3 ± 0.1)	216	(1.4 ± 0.1)	291	3.7
$r_d =$ 2.0 mm	Analytical	2.0	462	2.0	301	4.4
	Ray-tracing	1.5	—	1.5	—	—
	BPM	(2.1 ± 0.1)	482	(2.0 ± 0.1)	301	4.4
	Experiment	(2.0 ± 0.1)	361	(1.8 ± 0.1)	270	3.9

Data availability

The simulation and evaluation code used to generate the results presented is available upon request.

References

1. J. M. Girkin and M. T. Carvalho, "The light-sheet microscopy revolution," *J. Opt.* **20**(5), 053002 (2018).
2. B. Glover, J. Teare, and N. Patel, "The status of advanced imaging techniques for optical biopsy of colonic polyps," *Clin. Transl. Gastroenterol.* **11**(3), e00130 (2020).
3. H. Li et al., "500 M m field-of-view probe-based confocal micro-endoscope for large-area visualization in the gastrointestinal tract," *Photonics Res.* **9**(9), 1829 (2021).
4. B. A. Flusberg et al., "High-speed, miniaturized fluorescence microscopy in freely moving mice," *Nat. Methods* **5**(11), 935–938 (2008).
5. W. Zong et al., "Large-scale two-photon calcium imaging in freely moving mice," *Cell* **185**, 1240–1256.e30 (2022).
6. C. J. Engelbrecht, F. Voigt, and F. Helmchen, "Miniaturized selective plane illumination microscopy for high-contrast *in vivo* fluorescence imaging," *Opt. Lett.* **35**(9), 1413 (2010).
7. F.-D. Chen et al., "Implantable photonic neural probes for light-sheet fluorescence brain imaging," *Neurophotonics* **8**, 025003 (2021).
8. G. Matz, B. Messerschmidt, and H. Gross, "Design and evaluation of new color-corrected rigid endomicroscopic high NA GRIN-objectives with a sub-micron resolution and large field of view," *Opt. Express* **24**, 10987 (2016).
9. G. Matz et al., "Chip-on-the-tip compact flexible endoscopic epifluorescence video-microscope for *in-vivo* imaging in medicine and biomedical research," *Biomed. Opt. Express* **8**, 3329 (2017).
10. E. Pshenay-Severin et al., "Multimodal nonlinear endomicroscopic imaging probe using a double-core double-clad fiber and focus-combining micro-optical concept," *Light Sci. Appl.* **10**(1) (2021).
11. S. Bakas et al., "MEMS enabled miniaturized light-sheet microscopy with all optical control," *Sci. Rep.* **11**(1), 14100 (2021).
12. T. Vettenburg et al., "Light-sheet microscopy using an Airy beam," *Nat. Methods* **11**(5), 541–544 (2014).
13. L. Niu et al., "Generation of one-dimensional terahertz Airy beam by three-dimensional printed cubic-phase plate," *IEEE Photonics J.* **9**(4), 1–7 (2017).
14. F. O. Fahrbach, P. Simon, and A. Rohrbach, "Microscopy with self-reconstructing beams," *Nat. Photonics* **4**, 780–785 (2010).
15. H. Kafian et al., "Light-sheet fluorescence microscopy with scanning non-diffracting beams," *Sci. Rep.* **10**(1), 8501 (2020).
16. J. Nylk et al., "Enhancement of image quality and imaging depth with Airy light-sheet microscopy in cleared and non-cleared neural tissue," *Biomed. Opt. Express* **7**(10), 4021 (2016).
17. P. Piksarv et al., "Integrated single- and two-photon light sheet microscopy using accelerating beams," *Sci. Rep.* **7**(1), 1435 (2017).
18. Y. Taege, T. S. Winter, and Ç. Ataman, "A bi-axially accelerating Airy beam for miniaturized light-sheet microscopy," *Proc. SPIE* **12433**, 124330A (2023).
19. G. A. Siviloglou and D. N. Christodoulides, "Accelerating finite energy Airy beams," *Opt. Lett.* **32**(8), 979 (2007).

20. G. A. Siviloglou et al., "Observation of accelerating Airy beams," *Phys. Rev. Lett.* **99**(21), 23–26 (2007).
21. Y. Taege et al., "Design parameters for Airy beams in light-sheet microscopy," *Appl. Opt.* **61**(17) (2022).
22. J. Baumgartl, M. Mazilu, and K. Dholakia, "Optically mediated particle clearing using Airy wavepackets," *Nat. Photonics* **2**(11), 675–678 (2008).
23. N. K. Efremidis et al., "Airy beams and accelerating waves: an overview of recent advances," *Optica* **6**(5), 686 (2019).
24. R. P. Chen and C. F. Ying, "Beam propagation factor of an Airy beam," *J. Opt.* **13**(8), 085704 (2011).
25. Y. Hu et al., "Self-accelerating Airy beams: generation, control, and applications," *Springer Ser. Opt. Sci.* **170**, 1–46 (2012).
26. Y. Wen et al., "Tailoring accelerating beams in phase space," *Phys. Rev. A* **95**(2), 1–8 (2017).
27. M. Schmid, D. Ludescher, and H. Giessen, "Optical properties of photoresists for femtosecond 3D printing: refractive index, extinction, luminescence-dose dependence, aging, heat treatment and comparison between 1-photon and 2-photon exposure," *Opt. Mater. Express* **9**, 4564 (2019).
28. S. L. Schulz et al., "Design and evaluation of miniaturized high numerical aperture and large field-of-view microscope objectives with reduced field curvature," *Proc. SPIE* **12356**, 1235604 (2023).
29. Y. Taege et al., "A miniaturized illumination unit for Airy light-sheet microscopy using 3D-printed freeform optics," in *Imaging and Appl. Opt. Congr. 2022 (3D, AOA, COSI, ISA, pcAOP)*, Optica Publishing Group, Vancouver, BC, p. IW3C.1 (2022).
30. "Geometrical product specifications (GPS): surface texture: areal part 3: specification operators (ISO 25178-3:2012)," ISO 25178, British Standards Institution (2012).
31. P. Virtanen et al., "SciPy 1.0: fundamental algorithms for scientific computing in Python," *Nat. Methods* **17**, 261–272 (2020).

Yanis Taege received his BSc degree in physics from the University of Constance in 2017 and his MSc degree in applied physics from the University of Freiburg in 2019. Since 2020, he has been pursuing his PhD in the Laboratory for Micro-Optics at the University of Freiburg working on 3D micro- and nanofabrication of microendoscopic systems.

Tim Samuel Winter received his BSc degree in microsystems engineering from the University of Freiburg in 2020. He is currently pursuing his MSc degree in microsystems engineering at the University of Freiburg and Tampere University.

Sophia Laura Schulz received her BSc degree in optometry and her MEng degree in laser- and optotechnologies from Ernst Abbe University of Applied Sciences in Jena. She has been working for GRINTECH GmbH since 2020 and has been enrolled as a physics PhD student at Friedrich-Schiller University of Jena since 2021. Her main field of interest is the development and especially optical design of miniaturized systems for various biophotonics applications.

Bernhard Messerschmidt received his PhD in physics from Friedrich-Schiller University of Jena in 1998. Now, he is a managing director at GRINTECH in Germany and is also responsible for all R&D activities. His research focuses on biomedical optics, gradient index optics, and optical metrology.

Çağlar Ataman received his PhD in electrical engineering from Koç University, Istanbul, Turkey, in 2008, and worked as a postdoctoral researcher at École Polytechnique Fédérale de Lausanne, in Switzerland, between 2008 and 2012. From 2012 to 2021, he was a senior scientist at the Department of Microsystems Engineering of the University of Freiburg, Germany, where he has been an assistant professor since 2021, leading the Microsystems for Biomedical Imaging Laboratory.